Energy Storage Materials 71 (2024) 103630

Contents lists available at ScienceDirect

Energy Storage Materials

journal homepage: www.elsevier.com/locate/ensm

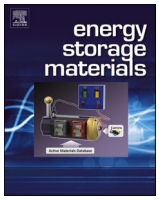

Polymer and Chaotropic Anion: A dual-additive strategy enables stable Zn Anode and high energy efficiency for Zn-Air/Iodide hybrid batteries

Siyuan Zhao [a,b,1], Jiayu Zhao [c,1], Wenlan Zhang [b], Yaping Yan [b], Jiachen Ma [b], Qinyang Feng [a], Idris Temitope Bello [a], Manhui Wei [e], Tong Liu [a,*], Jinhye Bae [c,d,*], Minshen Zhu [b,*], Meng Ni [a,*]

[a] Department of Building and Real Estate, Research Institute for Sustainable Urban Development (RISUD) and Research Institute for Smart Energy (RISE), The Hong Kong Polytechnic University, Hung Hom, Kowloon, Hong Kong, China
[b] Research Center for Materials Architectures and Integration of Nanomembranes (MAIN), Chemnitz University of Technology 09126 Chemnitz, Germany
[c] Department of NanoEngineering, University of California San Diego, La Jolla, CA 92093, USA
[d] Sustainable Power and Energy Center (SPEC), University of California San Diego, La Jolla, CA 92093, USA
[e] School of Mechanical Engineering, Beijing Institute of Technology 100081 Beijing, PR China

ARTICLE INFO

Keywords:
Electrolyte additive
Energy efficiency
Salting-in
Zn-air battery
Zn anode

ABSTRACT

The severe Zn dendrite growth and low energy efficiency inhibit the application of Zn-air batteries (ZABs) in energy storage. Electrolyte additives are promising to resolve these issues and improve battery performance. Polyacrylamide (PAM) additive with abundant polar functional groups can theoretically induce a uniform Zn deposition and interacts with water molecules to lower the water activity but suffer from limited effect in practice due to low solubility. Concurrently, chaotropic anion I^- with a lower oxidation potential is also introduced to substitute the sluggish oxygen evolution reaction (OER) with a faster iodide oxidation reaction (IOR) during charging, contributing to a Zn-air/iodide hybrid battery with enhanced energy efficiency. However, the I^- has no effect on Zn dendrite issues. Herein, we develop a dual-additive strategy employing polymer and chaotropic anion simultaneously to take both their advantages but also avoid the drawbacks. I^- can facilitate the dissolution and untangling of PAM chains, which enables more functional groups to interact with Zn and water molecules. Thanks to the synergetic effect of PAM and I^-, the hybrid ZAB delivers a long cycle life of 240 h with a high energy efficiency of 74.6 % and obtains a stable Zn anode with alleviated dendrite growth and improved utilization rate. Moreover, the rapid IOR process enables stable battery operation at -20 °C, further broadening the application scenarios of ZABs.

1. Introduction

Advanced electrochemical energy storage technologies play a crucial role in the way to carbon neutrality [1-4]. Among them, Zn-air batteries (ZABs) are promising candidates due to their inherent safety, high energy density, and cost-effectiveness [5-7]. Since their birth in 1878, ZABs have experienced 140 years of development [8,9]. Regretfully, nowadays, apart from being employed in some tiny electronic devices, ZABs almost disappear from the market, let alone energy storage applications [10,11]. One of the facts is the energy efficiency of ZABs is only 60 %, which cannot meet the requirement of energy storage (generally > 70 %) [12-14]. Another critical issue lies in the Zn metal inevitably suffers from parasitic hydrogen evolution reaction (HER) and dendrite growth, leading to low Zn utilization rate and restricted battery lifetime [15-17].

The low energy efficiency in ZABs is primarily due to the high charging voltage (~2 V), a result of the intrinsically sluggish four-electron oxygen evolution reaction (OER) process [18,19]. Despite huge efforts to enhance the OER catalytic activity, the charging voltage still failed to lower below 1.9 V [20,21]. Recently, researchers thought out of the box to employ reaction modifiers (RMs) with lower oxidation potential and faster kinetics to substitute the OER process [22,23]. This way, the ZAB converts to a Zn-air/RM hybrid battery, allowing the charging voltage to be reduced to ~1.7 V, and achieving an energy efficiency of over 70 % [24,25].

Although these RMs can switch the cathodic reaction and improve

* Corresponding authors.
E-mail addresses: tongliu@polyu.edu.hk (T. Liu), j3bae@ucsd.edu (J. Bae), minshen.zhu@etit.tu-chemnitz.de (M. Zhu), meng.ni@polyu.edu.hk (M. Ni).
[1] These authors contributed equally to this work.

https://doi.org/10.1016/j.ensm.2024.103630
Received 21 April 2024; Received in revised form 26 June 2024; Accepted 7 July 2024
Available online 10 July 2024

the battery energy efficiency, there is no report claiming they are able to address the Zn side issues (Scheme 1). To alleviate the dendrite growth and parasitic HER, researchers have proposed various strategies to stabilize the Zn anode, including battery structure optimization, anode modification, and electrolyte additive engineering [26-28]. Among these strategies, introducing electrolyte additives is considered simple and low-cost [29]. Soluble polymer additives are particularly attractive because of their plentiful hydrophilic functional groups on the polymer chains [30,31]. Theoretically, these functional groups can not only induce a uniform Zn deposition but also interact strongly with water molecules to mitigate parasitic HER [32,33]. Unfortunately, in practical application, the solubility of these polymer additives is not satisfied and most polymer chains are still in an entangled state, exposing limited function groups and hence demonstrating limited positive effect [34]. Moreover, the swelling polymer additives with entangled chains own a high viscosity, which further lowers the electrolyte ionic conductivity (Scheme 1) [35]. Recently, a series of anions have been incorporated into polymer hydrogels to modulate their mechanical properties by affecting the solubility and aggregation state of polymer chains, which is an application of Hofmeister effect [36]. The Hofmeister effect divides the ion species into chaotropic ions and kosmotropic ions [37]. Chaotropic ions disrupt the hydrogen bonding (HB) among water molecules and enable the dissolution of polymer chains, whereas kosmotropic ions induce the opposite effect [38,39]. It is also worth mentioning anions exert a more pronounced influence than cations [40]. Consequently, the concurrent utilization of polymers and chaotropic anions could theoretically yield superior results compared to the exclusive use of the polymer additive, although requiring further validation. On the other hand, it is also regretful that these polymer additives fail to improve the energy efficiency of ZABs.

Regretfully, the current reported strategies can only unilaterally elevate the energy efficiency or stabilize the Zn anode of ZABs. The truth is only if both energy efficiency and stable Zn anode are achieved simultaneously can ZABs show in energy storage application. Therefore, here we develop a dual-additive strategy for ZABs to simultaneously achieve high energy efficiency, mitigated Zn dendrite growth, and suppressed parasitic HER (Scheme 1). We employ polyacrylamide (PAM) with hydrophilic amide groups as the polymer additive for stabilizing the Zn anode. Concurrently, I^- is introduced as the RM to replace the sluggish OER by a more rapid I^- oxidation reaction (IOR) process. In addition, I^- breaks the HB among water molecules and lowers the water activity, alleviating the undesirable parasitic HER. More importantly, by Hofmeister effect, I^- interacts intimately with PAM chains and facilitates their untangling and dissolution, leading to more exposure of polar functional groups and reduction of electrolyte viscosity. Consequently, a highly stable Zn anode can be achieved, accompanied by a diminished impact on the electrolyte ionic conductivity. By the synergetic effect of the two additives, the hybrid Zn-air/iodide battery displays a high energy efficiency of 74.6 %, an extended lifetime of 240 h, and a stable Zn anode with alleviated dendrite growth and improved utilization rate. Besides, the swift IOR process also enables the stable operation of the hybrid ZABs in a -20 °C environment, further extending their application scenarios. This dual-additive strategy offers new insights into additive engineering and promotes the practical application of ZABs in energy storage. It is also believed this strategy will hold significant potential for application in various aqueous metal-ion and metal-air battery systems.

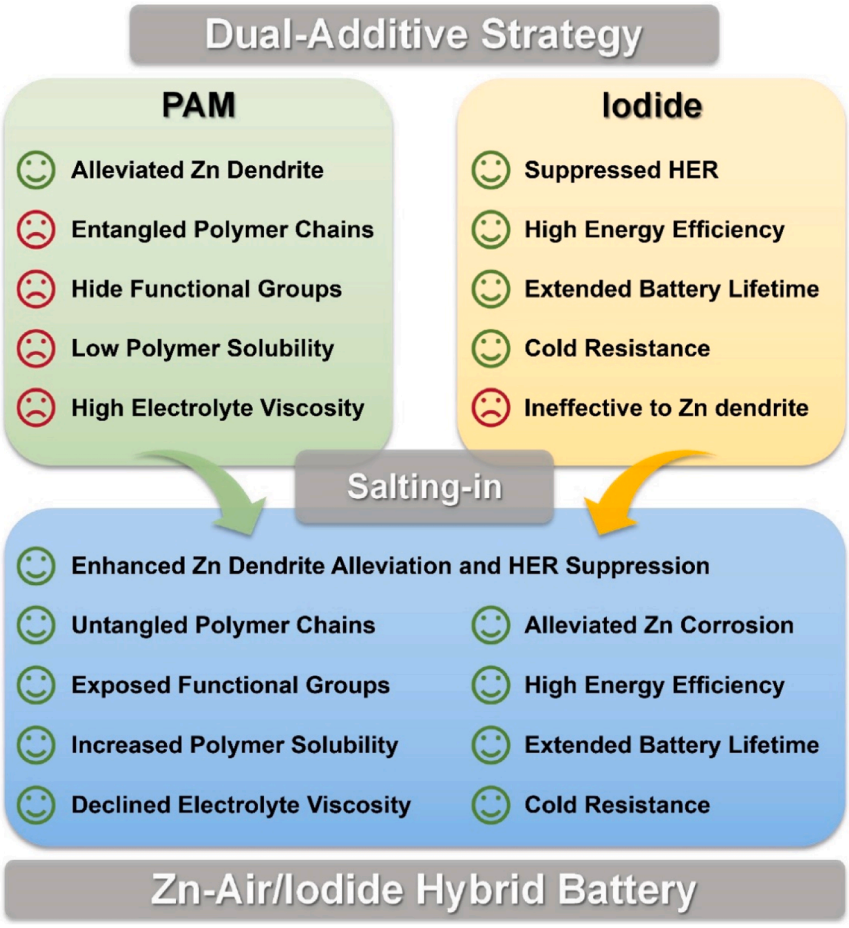

Scheme 1. PAM and iodide dual-additive strategy for Zn-air/iodide hybrid batteries.

2. Results and discussion

2.1. Interactions among PAM, KI, and KOH electrolyte

Generally, ZABs employ alkaline solutions as the electrolyte. According to the previous study, electrolytes with 4 M KOH and 2 M KI can enable impressive electrochemical performances for ZABs, and 5 wt. % PAM can effectively alleviate Zn side issues while much higher concentration PAM will harm the battery performances [22,41]. Therefore, in this work, we select 4 M KOH, 2 M KI, and 5 wt. % PAM and denote as KOH, KI, and PAM throughout, unless otherwise specified.

Fourier transform infrared spectroscopy (FTIR) is used to characterize the PAM state in the KOH + KI + PAM electrolyte. As shown in Fig. 1a, all the samples exhibit a strong peak at around 1600-1650 cm^{-1}, which indicates the O-H bending vibration of water molecules [42]. This peak is so strong and covers the characteristic peak of the amide group $CONH_2$ in PAM [43]. Since there is no functional group in the KOH + KI solution, no other peak is observed. After dissolving PAM in KOH + KI solution, the C-N stretching (~1441 cm^{-1}) blueshifts, and the intensity decreases, indicating the diminish of $CONH_2$ groups [44]. Besides, two new peaks emerge at 1556 and 1406 cm^{-1}, demonstrating the formation of the carboxyl group COO^- and alkalified PAM (APAM) [45]. Fig. 1b depicts the PAM alkalinization process for a better understanding. In an alkaline environment, $CONH_2$ partially turns to COO^- from the nucleophilic attacks by hydroxide ions OH^- [46]. This process is also accompanied by the release of NH_3 gas, which can be confirmed by the continuously diffusing smell from the KOH + KI + PAM electrolyte. According to the density functional theory (DFT) calculation in Fig. S1, the binding energy of APAM-H_2O is much higher than that of H_2O-H_2O, illustrating water molecules own a strong tendency to interact with APAM. Besides, because COO^- is more hydrophilic and has larger polarity than $CONH_2$, the binding energy of APAM-H_2O is higher than that of PAM-H_2O, suggesting APAM enjoy superior capability in HER suppression than the pristine PAM [45].

However, the effectiveness of APAM is significantly restricted by the entangled polymer chains. As shown in Fig. 1c, these polymer chains aggregate together by HB from the APAM function groups, leaving very limited space for water molecules [39]. This causes a low solubility of APAM, which in turn leads to an increased viscosity. So far, the electrolyte containing APAM cannot be regarded as a polymer solution because the polymer swelling dominates rather than dissolution. Moreover, since the HB network among water molecules is hardly interrupted by the entangled APAM chains, the reduction of water activity is limited. I^- can untangle the APAM chains and enable their dissolution. According to the Hofmeister effect, chaotropic anions like I^- own a strong interaction with APAM chains, which is supported by the DFT calculation in Fig. 1d. This strong interaction facilitates the insertion of I^- into APAM chains to break the inner polymeric HB network [47]. Without the link by inner HB, the entangled APAM chains get released, exposing more free $CONH_2$ and COO^- functional groups to interact with water molecules and other ions like $Zn(OH)_4^{2-}$. The enhanced interplay between APAM chains and water molecules by I^- further enables the dissolution of APAM chains, which is called salting-in [48]. As a result, the viscosity of the KOH + PAM + KI electrolyte (untangled APAM) significantly reduced to 3129 cp from 5356 cp of the KOH + PAM electrolyte (entangled APAM) (Fig. 1e). Correspondingly, the ionic conductivity of the KOH + PAM + KI electrolyte increases, which can be reflected in the reduced electrolyte resistance from the alternating current (AC) impedance spectra (Fig. 1f). In addition, the decreased viscosity also helps build a more intimate electrode-electrolyte interface and reduce the interfacial charge transfer resistance, as displayed in the smaller radius of the semicircle (Fig. 1f) [49]. Thanks to I^-, the positive effect of APAM can be unleashed and the negative effect is diminished. Moreover, as an intrinsically chaotropic anion, the I^- itself can break the HB network among water molecules by generating the H_2O-I^- interaction (Fig. 1d), further suppressing the water activity and alleviating parasitic HER [50].

2.2. Individual and synergetic effects of APAM and KI on water molecules

To gain a deeper understanding of the individual and synergetic effects of APAM and KI on water molecules, FTIR characterization is conducted to reveal the water states in KOH, KOH + PAM, KOH + KI, and KOH + PAM + KI electrolytes. As shown in Fig. 2a, the wide peaks corresponding to the O-H stretching vibration of water molecules gradually blueshift with the addition of PAM and KI. This phenomenon indicates that either APAM or KI can interact with water molecules and show enhanced effects when they both exist [51]. To further investigate in what extent APAM and KI interact with water molecules, the peaks of O-H stretching vibration are fitted and divided into three components, namely the strong HB (at ~3230 cm^{-1}, SHB) and weak HB (at ~3410 cm^{-1}, WHB) among water molecules, and other bonds (at ~3570 cm^{-1}, OB) between water molecules and APAM/I^- (Fig. 2b) [52]. Fig. 2b also provides the detailed area ratio corresponding to the fitted FTIR spectra. With the introduction of PAM, the ratio of the OB (HB between APAM and water molecules) just increases slightly, demonstrating the entangled APAM chains expose less polar functional groups and have limited interaction on water molecules. On the other hand, the ratio of the SHB (HB among water molecules, the same below) also decreases marginally, indicating the entangled APAM can hardly break the water structure. For the KOH electrolyte with KI, it shows a greater extent in increasing the OB (interaction between I^- and water molecules) ratio and decreasing the SHB ratio due to the strong chaotropic ability of I^-. When PAM and KI are simultaneously introduced in the KOH electrolyte, ratios of the OBs (interactions between water molecules and APAM/I^-) and the SHB significantly increases and decreases, respectively. This result demonstrates I^- can unleash the potential of APAM in interacting with water molecules and form a greater synergetic effect with APAM to weaken the HB among water molecules. ^1H nuclear magnetic resonance (NMR) is also conducted to characterize the water structure in the above electrolytes. As shown in Fig. 2c, ^1H peaks of KOH electrolytes with PAM, KI, and PAM + KI shift to lower fields in sequence, manifesting the disruption of HB among water molecules also get enhanced accordingly [52]. The results from ^1H NMR spectra correspond well to the FTIR spectra and further support that the polymer APAM and chaotropic anion I^- can generate synergetic effect to suppress the water activity.

Since ZABs are a semi-open system, the electrolyte will inevitably evaporate from the porous air cathode. Therefore, a good water retention ability is crucial for the normal operation of ZABs. As shown in Fig. S2, the KOH electrolyte can only retain 83 % water after exposure in the atmosphere for a week (25 °C and 60 % relative humidity). In sharp contrast, the optimized KOH + PAM + KI electrolyte can achieve 90 % water retention, attributing to the depressed water activity by APAM and KI. The lower water activity suggests the water-induced parasitic HER is also alleviated. As the linear sweep voltammetry (LSV) curves in Fig. 2d exhibited, the HER onset potential of the KOH electrolyte moves to more negative region with the addition of PAM, KI, and PAM + KI. The expanded negative part of the electrochemical stability window decreases the risk of H_2 generation on the Zn anode. Accordingly, from the Tafel plots in Fig. 2e, the Zn anode exhibits an improved corrosion resistance in the KOH + PAM + KI electrolyte as the most positive corrosion potential is observed. Besides, the corrosion current density also reduced from 0.44 $mAcm^{-2}$ in the KOH electrolyte to 0.30 mA cm^{-2} in the KOH + PAM + KI electrolyte, illustrating the corrosion on the Zn anode decelerates. The tendency of the electrochemical results corresponds well to the characterization of the water structure in these electrolytes, demonstrating the synergetic effect of APAM and KI can simultaneously alleviate Zn corrosion and parasitic HER by lowering water activity.

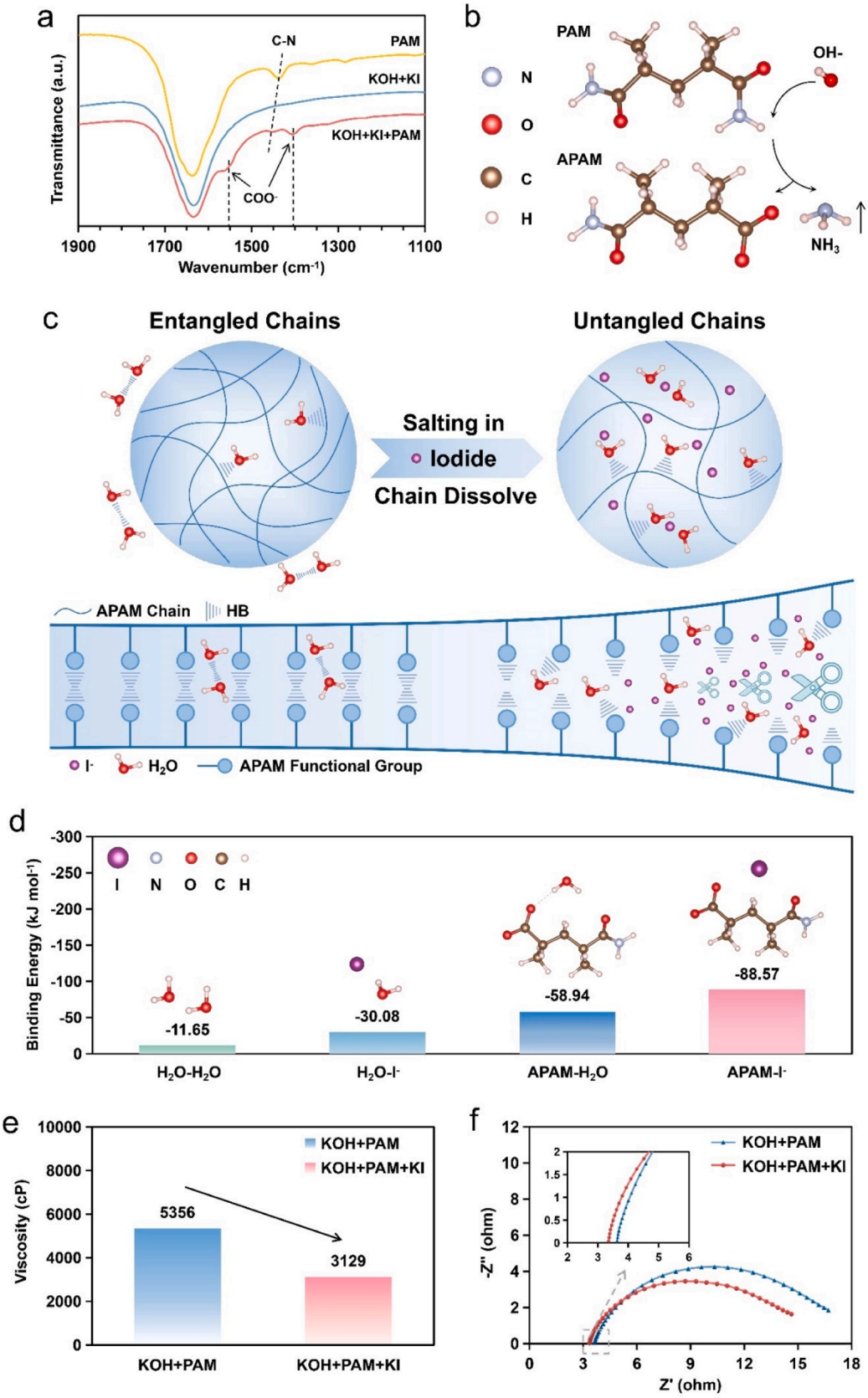

9

Fig. 1. Interactions among PAM, KI, and KOH electrolyte. (a) FTIR spectra of the PAM, KOH + KI, and KOH + KI + PAM solutions. (b) Schematic of the alkalinization process of PAM. (c) Schematic of the salting-in process of APAM chains by chaotropic anion I-. (d) Binding energies of the H_2O-H_2O, H_2O-I^-, APAM-H_2O, and APAM-I^-. (e) Viscosities of the KOH + PAM and KOH + PAM + KI electrolytes. (f) AC impedance of the ZABs with KOH + PAM and KOH + PAM + KI solutions.

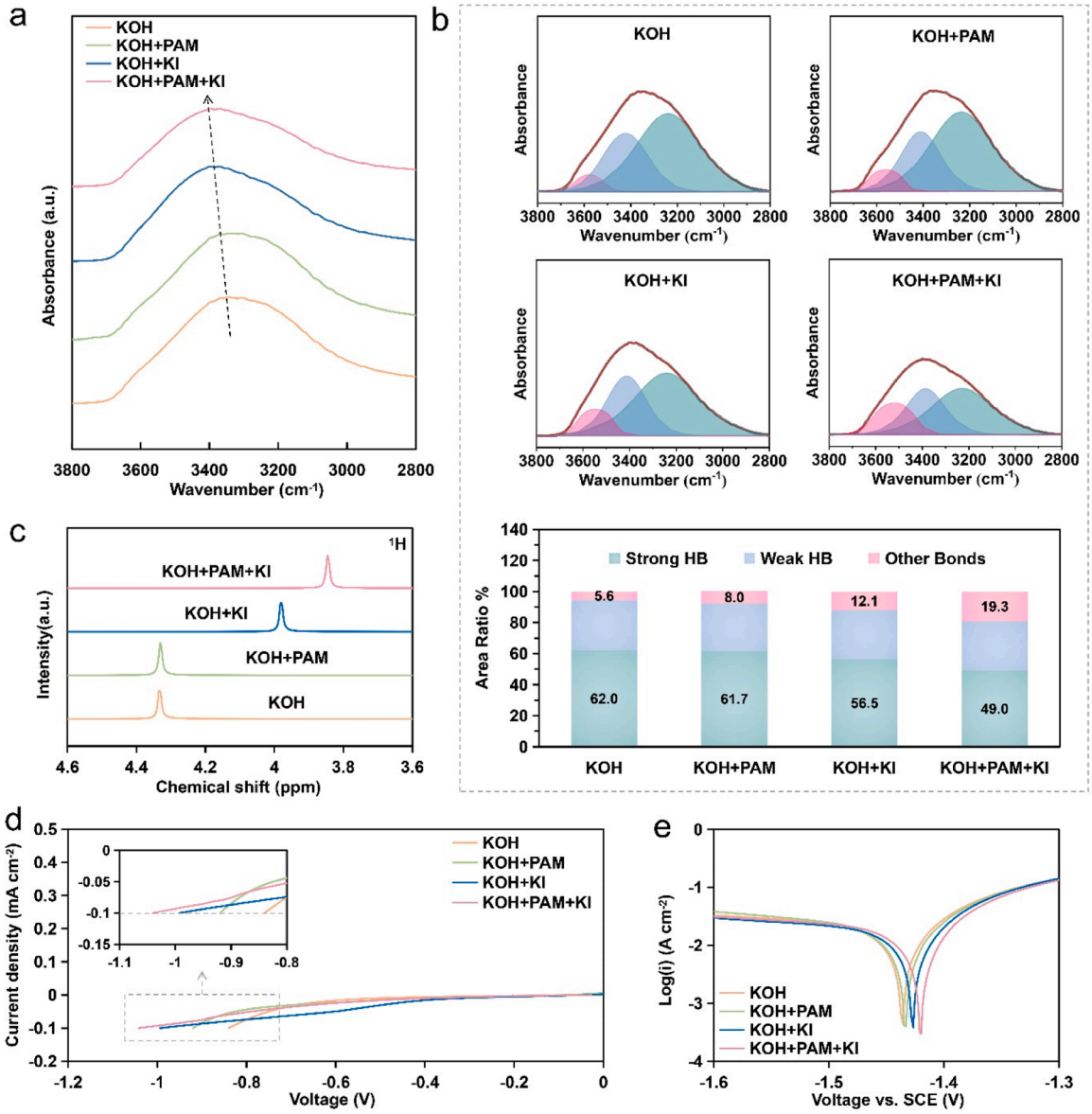

Fig. 2. Individual and synergetic effects of APAM and KI on water molecules. (a) FTIR spectra of the O-H stretching vibration of water molecules. (b) Fitted FTIR spectra and the area ratio of strong HB, weak HB, and other bonds. (c) ^{1}H NMR spectra of water molecules. (d) The negative part of the electrochemical stability window. (e) Tafel plots of the Zn anode. The used electrolytes are KOH, KOH + PAM, KOH + KI, and KOH + PAM + KI.

2.3. Individual and synergetic effects of APAM and KI on Zn dendrite

To investigate how APAM and KI will affect the Zn deposition behavior in the KOH electrolyte, we first conduct the chronoamperometry (CA) of potentiostatic Zn plating at -1.8 V. As shown in Fig. 3a, all the CA curves present an L-shape, and the current density experiences a sudden drop from a high level and then decreases to a relatively low range. This indicates the Zn deposition is a typical diffusion-controlled process [53]. Fig. 3b further shows the initial period in detail. The Zn deposition starts at a high current density but without the process from 0 to maximum, suggesting the Zn nucleation process is transient [53]. Within the first 0.5 s, the Zn in the KOH electrolyte delivers an initial current density of 161 mA cm^{-2}, indicating the nucleation sites on the Zn surface are activated. For the Zn in the KOH + KI electrolyte, the initial current density is 159 mA cm^{-2}, demonstrating the I^- will hardly affect the nucleation. However, in the case of KOH + PAM and KOH + PAM + KI electrolytes, both initial current densities significantly decrease to 82 and 79 mA cm^{-2}, respectively. This phenomenon is mainly due to the strong adsorption of APAM chains on the Zn surface (Fig. S3 and Fig. S4), reducing the surface activation of Zn nucleation.

After nucleation, the deposited Zn begins to grow. From Fig. 3b, the current density gradually diminishes due to the overlapping diffusion zones created by the nuclei distributed on the Zn substrate, as well as the concentration reduction of active Zn^{2+} ions on the Zn surface [53]. After ~5 s, the current density converges at a constant platform. Back to Fig. 3a, for the KOH and KOH + KI electrolytes, both the CA curves show a distinct inflection point, after which the deposition current density undergoes a monotonic increase. The increase manifests the Zn anode is exposing more and more surface area owing to the porous and dendritic metallic Zn deposition. In addition, the similar results of KOH and KOH + KI electrolytes also suggest that I^- exerts little influence in alleviating Zn dendrite formation. This might be because Zn^{2+} ions exist in the form of $Zn(OH)_4^{2-}$ in alkaline solutions hence I^- can hardly affect the Zn^{2+} solvation structure [50]. Luckily, the PAM additive can effectively mitigate the dendrite issue. In Fig. 3a, the KOH + PAM electrolyte displays a stable current profile without apparent increase, demonstrating the Zn deposition is dense and uniform. After the addition of KI, APAM chains are untangled and distributed more evenly on the Zn surface. As a

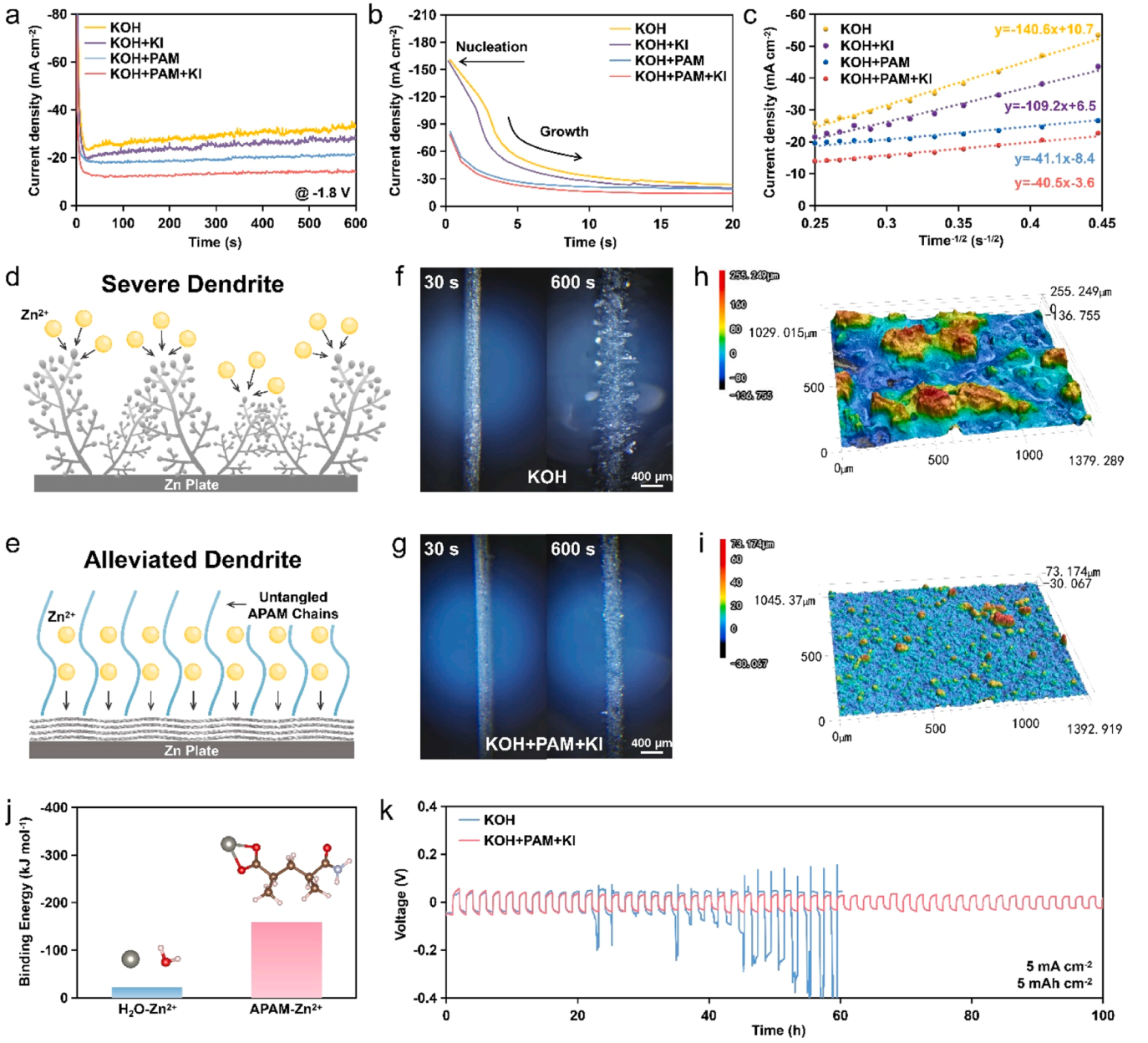

Fig. 3. Individual and synergetic effects of APAM and KI on Zn dendrite. (a) Chronoamperometry profiles of Zn deposition at -1.8 V and (b) their first 20 s behavior and (c) their j-$t^{-1/2}$ relationship in KOH, KOH + PAM, KOH + KI, and KOH + PAM + KI electrolytes. (d)-(e) Schematic, (f)-(g) Microscopic images, and (h)-(i) CLMS images of the Zn deposition in KOH and KOH + PAM + KI electrolytes. (j) Binding energies of the H_2O-Zn^{2+} and APAM-Zn^{2+}. (k) Cycling performance of Zn//Zn symmetric cells at 5 mA cm^{-2} and 5 mAh cm^{-2} in KOH and KOH + PAM + KI electrolytes.

result, the current profile of the KOH + PAM + KI electrolyte becomes flatter. Moreover, the current density declines at the same time, indicating the Zn deposition kinetics is suppressed [54]. We also notice that the deposition curves of electrolytes without PAM show less smooth than that of electrolytes containing PAM, which suggests the Zn dendrite growth is more reckless without the induction of PAM.

Since the Zn deposition process is the diffusion-controlled process, the current density and time follow the Sand equation [55]:

$$j = \frac{nFC(D\pi)^{\frac{1}{2}}}{2} t^{-\frac{1}{2}}$$

where j is the current density, n is the number of electrons, F is the Faraday constant, C is the concentration, D is the diffusion coefficient, and t is the time. Because n, F, and C are constants, we can compare the diffusion coefficient of Zn^{2+} ions (D) in various electrolytes by the experimentally acquired j and t. This will provide a supplementary understanding of how APAM and I^- influence the diffusion process of Zn^{2+} ions. As plotted in Fig. 3c, a significant difference is observed between the slopes with and without PAM addition. This result further suggests the APAM chains can interact with Zn^{2+} ions to slow down their transfer and restrict the deposition kinetics.

From the above discussion, it is evident that the Zn deposition is more rapid and disordered without APAM. In addition, charges tend to accumulate at the tips of the deposited Zn, accelerating the dendrite growth (Fig. 3d). When under the induction of APAM, the polymer chains act as the carrier of Zn^{2+} transfer and enable a uniform Zn deposition (Fig. 3e). The existence of I^- also amplifies the effect of APAM, further alleviating the dendrite growth. Combined with the evidence in suppressing water activity, we can conclude there is indeed a positive synergetic effect of PAM and KI.

Apart from the electrochemical illustration, the images of the deposited Zn anode are also presented. In the case of the KOH electrolyte, the deposited Zn exhibits a loose state in the first 30 s and forms severe dendrites at the end of deposition (600 s), as shown in Fig. 3f. The increased surface area will also cause the parasitic HER to occur more readily. In sharp contrast, the deposition in the KOH + PAM + KI electrolyte is uniform and dense in the early stage, and no obvious dendrite is observed after deposited for 600 s (Fig. 3g). Moreover, 3D laser scanning microscopy is also employed to characterize the morphology of the Zn surface. As shown in Fig. 3h, the Zn plate shows a rough surface with distinct dendrites in the KOH electrolyte. However, the Zn morphology in the KOH + PAM + KI electrolyte is smoother and exhibits less fluctuation, demonstrating the dendrite formation is significantly alleviated by the addition of PAM and KI (Fig. 3i). The observation on the deposited Zn surface also corresponds well with the electrochemical profiles.

Furthermore, the DFT calculation is also conducted to support the experimental results. As shown in Fig. 3j, the interaction between Zn^{2+} ions and APAM is significantly stronger than that between Zn^{2+} ions and water molecules, indicating the Zn^{2+} ions will be adsorbed on APAM chains (polar functional groups), and their transfer kinetics is suppressed. Moreover, according to the calculation results in Fig. S3 and Fig. S4, APAM chains adsorb on the Zn surface by polar functional groups, which can provide uniform electric field and Zn^{2+} ion distribution, further facilitating the uniform Zn deposition.

Finally, we fabricate a Zn//Zn symmetric cell to evaluate the cycle stability of Zn plate in different electrolytes at 5 mA cm^{-2} and 5 mAh cm^{-2}. As shown in Fig. 3k, the deposition overpotential in the KOH + PAM + KI electrolyte is slightly higher than in the KOH electrolyte. Besides, from the cathodic voltammetry scanning, a more negative Zn reduction peak is also observed in the KOH + PAM + KI electrolyte (Fig. S5). These phenomena can be ascribed to the adsorption of APAM on the Zn surface and the interaction with Zn^{2+} ions, which consequently retards the reckless Zn deposition. In addition, in the KOH electrolyte, the Zn anode becomes unstable after 20 h and followed with fierce voltage fluctuation, suggesting severe dendrite growth and parasitic HER process on the Zn surface. The cell finally fails because of the short circuit by the dendrite touch (Fig. S6). In comparison, the cell in the KOH + PAM + KI electrolyte operates stably, extending the cycle life to over 100 h.

2.4. ZAB performances at 25 °C

From the previous study, the electrochemical reactions within Zn-air/iodide hybrid batteries have been well illustrated as [24,56]:

Anodic reaction (discharging and charging):

$$Zn + 4OH^- \rightleftharpoons Zn(OH)_4^{2-} + 2e^-$$

Cathodic reduction reaction (discharging):

$$O_2 + 2H_2O + 4e^- \rightarrow 4OH^-$$

Cathodic oxidation reaction (charging):

$$2I^- - 2e^- \rightarrow I_2(Electrochemical)$$

$$3I_2 + 6OH^- \rightarrow 5I^- + IO_3^- + 3H_2O(Chemical)$$

During battery charging, the IOR process dominates on the cathode because of its lower oxidation potential and faster kinetics. The I^- is first oxidized as I_2, which is unstable in the alkaline environment and then disproportion to I^- and IO_3^-. In the discharging process, the reduction of IO_3^- can be neglected when oxygen is sufficient, indicating that the ORR process is prominent on the cathode. As for the anode reactions, those are the Zn dissolution and deposition.

A series of electrochemical tests are then performed to evaluate the effect of the KOH + PAM + KI electrolyte in ZABs. As shown in Fig. S7, for the KOH electrolyte, the LSV profile of OER starts at a high potential of 0.77 V vs. SCE (at 10 mA cm^{-2}) and ends at a current density of 101 mA cm^{-2}. In sharp contrast, the onset potential and end current of the KOH + PAM + KI decrease to 0.44 V vs. SCE and increase to 190 mA cm^{-2}, respectively. This result indicates the IOR with lower oxidation potential and faster two-electron-transfer can substitute the sluggish OER process [57]. Consequently, the charge voltage of ZABs with the KOH + PAM + KI electrolyte (abbreviated as hybrid ZABs) also declines correspondingly, as illustrated in Fig. 4a. By merits of KI, the charging voltage immediately achieves a stable platform, while the ZAB using KOH electrolyte (abbreviated as conventional ZABs) experiences a longer period to become stable. Moreover, we also notice that the voltage reduction at 1 mA cm^{-2} is ~0.28 V and enlarges to ~0.36 V at 20 mA cm^{-2}, demonstrating the advantage of KI in high-current fast charging. Although KI will cause a decrease in discharge voltage due to its adsorption on the catalytic active sites, the impact is little, and the discharge voltages of the two ZABs are very close [24]. Thanks to the significant reduction in charging voltage, the energy efficiency enjoys an exceptional improvement. As presented in Fig. 4b, in the case of hybrid ZABs, the energy efficiency reaches over 80 % at 1 mA cm^{-2}. Even at 20 mA cm^{-2}, the energy efficiency is still near 70 %. For conventional ZABs, the energy efficiency is unable to reach 70 % at 1 mA cm^{-2}, far from the requirement of energy storage. Apart from the high energy efficiency, the hybrid ZAB also displays a notably high peak power density of 110 mW cm^{-2}, very close to the conventional ZAB of 118 mW cm^{-2} (Fig. 4c). During the discharge process, both ZABs exhibit a stable discharge platform with an average voltage of ~1.25 V at 5 mA cm^{-2} (Fig. 4d). In addition, the hybrid ZAB shows a higher specific capacity of ~790 mAh g^{-1} (Zn utilization rate of ~96.3 %) than the conventional ZAB, indicating less parasitic HER and Zn corrosion due to the depressed water activity.

Finally, the rechargeability and cycling performance are evaluated, as illustrated in Fig. 4e. Unlike other ZAB studies using a short-period cycling protocol like 20 min $cycle^{-1}$, we employ 2 h $cycle^{-1}$ to meet the requirement of practical applications. For the conventional ZAB, the charging voltage quickly rises to a high platform of ~2.1 V at 5 mA cm^{-2}, and the cycling finally stops at ~60 h. The reason of battery failure lies in the Pt/C catalyst deterioration under a high charging voltage, which continuously corrodes the carbon support and causes the loss of Pt nanoparticles. The severe carbon corrosion can also get confirmed from the electrolyte color change from colorless to brown (Fig. S8). In sharp contrast, the hybrid ZAB shows an impressive charging voltage of ~1.7 V and energy efficiency of 74.6 % at 5 mA cm^{-2}. Moreover, the battery can stably cycle for over 240 h. The considerably extended cycle life originates from the alleviation of catalyst corrosion (Fig. S8), which is also the result of lower charging voltage by IOR as proven in our previous research [24,56]. The presented battery performances are competitive or superior to other studies with RMs (Table S1), let alone conventional ZABs. Further combined with the merits of alleviated parasitic HER and dendrite formation, it is believed this dual-additive strategy with multi-functions has great potential to facilitate the commercialization of ZABs.

2.5. ZAB performances at -20 °C

A wider operating temperature range can further expand the application scenarios of ZABs. Therefore, the battery performances at -20 °C are also evaluated. Generally, in such a cold environment, the electrolyte may suffer from freezing, and the electrocatalytic activity declines [58]. Luckily, both the KOH and KOH + PAM + KI electrolytes can remain in an unfrozen liquid state because of the high alkaline concentration (Fig. S9) [59]. Besides, benefiting from the excellent oxygen reduction reaction (ORR) electrocatalytic activity of Pt/C, the discharge performances of the two batteries are hardly affected by the cold temperature (Fig. 5a). However, the OER electrocatalytic activity of Pt/C is poor and more susceptible to performance degradation in the -20 °C environment. Hence, the conventional ZAB suffers from a noticeable

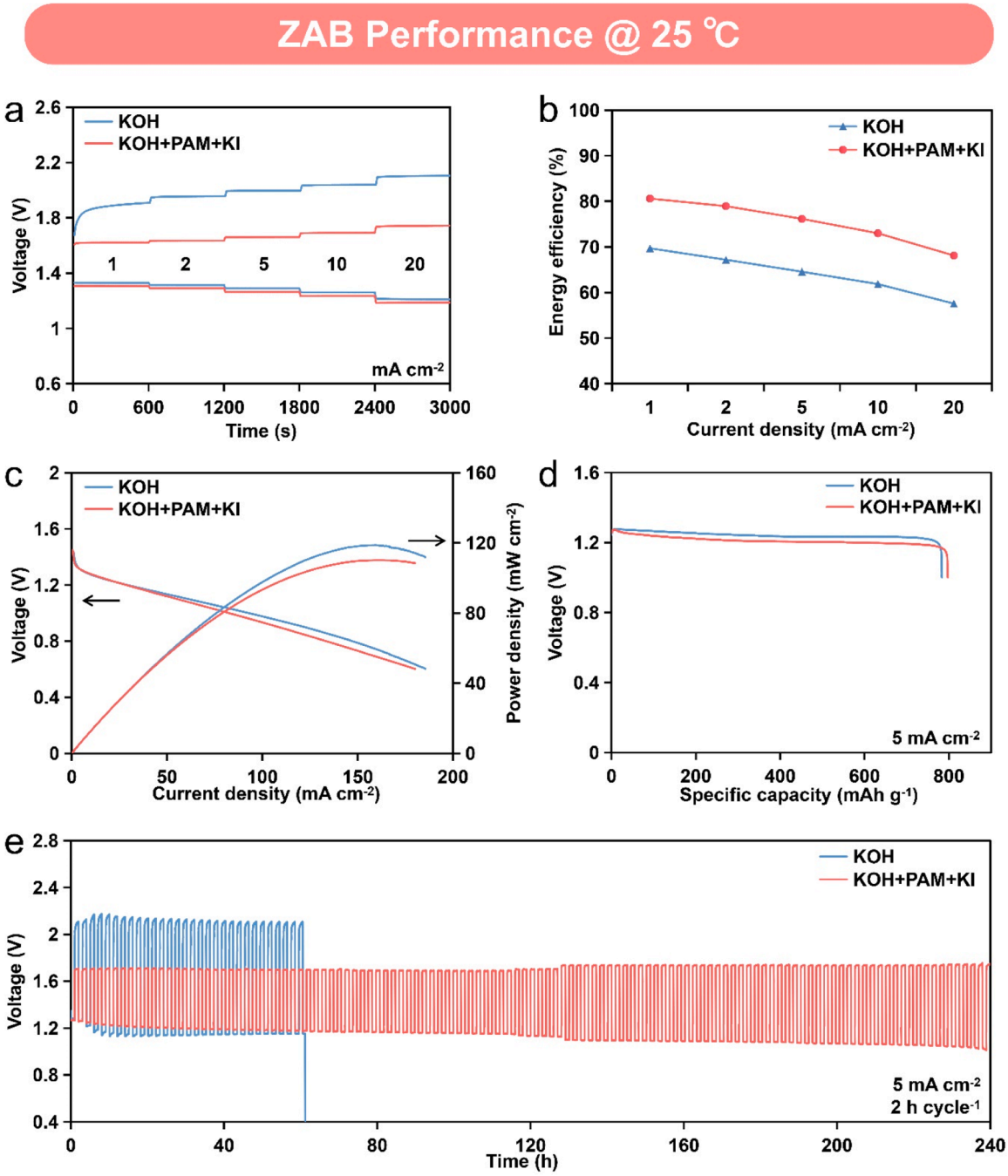

Fig. 4. Electrochemical performances of ZABs at 25 °C. (a) Charge and discharge voltages and (b) corresponding energy efficiencies at 1, 2, 5, 10, 20 mA cm^{-2}. (c) Discharge polarization profiles with corresponding power densities. (d) Discharge profiles at 5 mA cm^{-2}. (e) Galvanostatic cycling profiles at 5 mA cm^{-2} and 2 h $cycle^{-1}$. The used electrolytes are KOH and KOH + PAM + KI.

increase in charging voltage (Fig. 5a), and the energy efficiency decreases correspondingly (Fig. 5b). However, for the hybrid ZAB, only a slight increase in charging voltage is observed, indicating the IOR process with fast kinetics can effectively resist the cold temperature (Fig. 5a). Accordingly, the energy density at 10 mA cm^{-2} is still as high as 70 %, significantly exceeding the ~54 % of the conventional ZAB (Fig. 5b). Moreover, in the -20 °C environment, not only the power density is retained at ~104 mW cm^{-2} (Fig. 5c) but also the average discharge voltage is still at a high level of ~1.2 V at 5 mA cm^{-2} (Fig. 5d), very close to those at 25 °C. For the crucial cycle performance, the ZAB with KOH electrolyte fails only after 40 h due to the high charging voltage at -20 °C (Fig. 5e). Thanks to the brilliant cold resistance of the KOH + PAM + KI electrolyte, the hybrid ZAB starts with an energy efficiency of 73.6 % and stably operate for over 200 h, exhibiting potential applications in extremely cold environments. Furthermore, when compared to other documented cases of ZABs operating at -20 °C, our hybrid ZAB exhibits superior electrochemical performances (Table S2). It is worth mentioning that due to the test machine limitation, the minimum testing temperature is -20 °C. However, considering the impressive performances at -20 °C, we believe this hybrid ZAB is capable to operate at a much lower temperature.

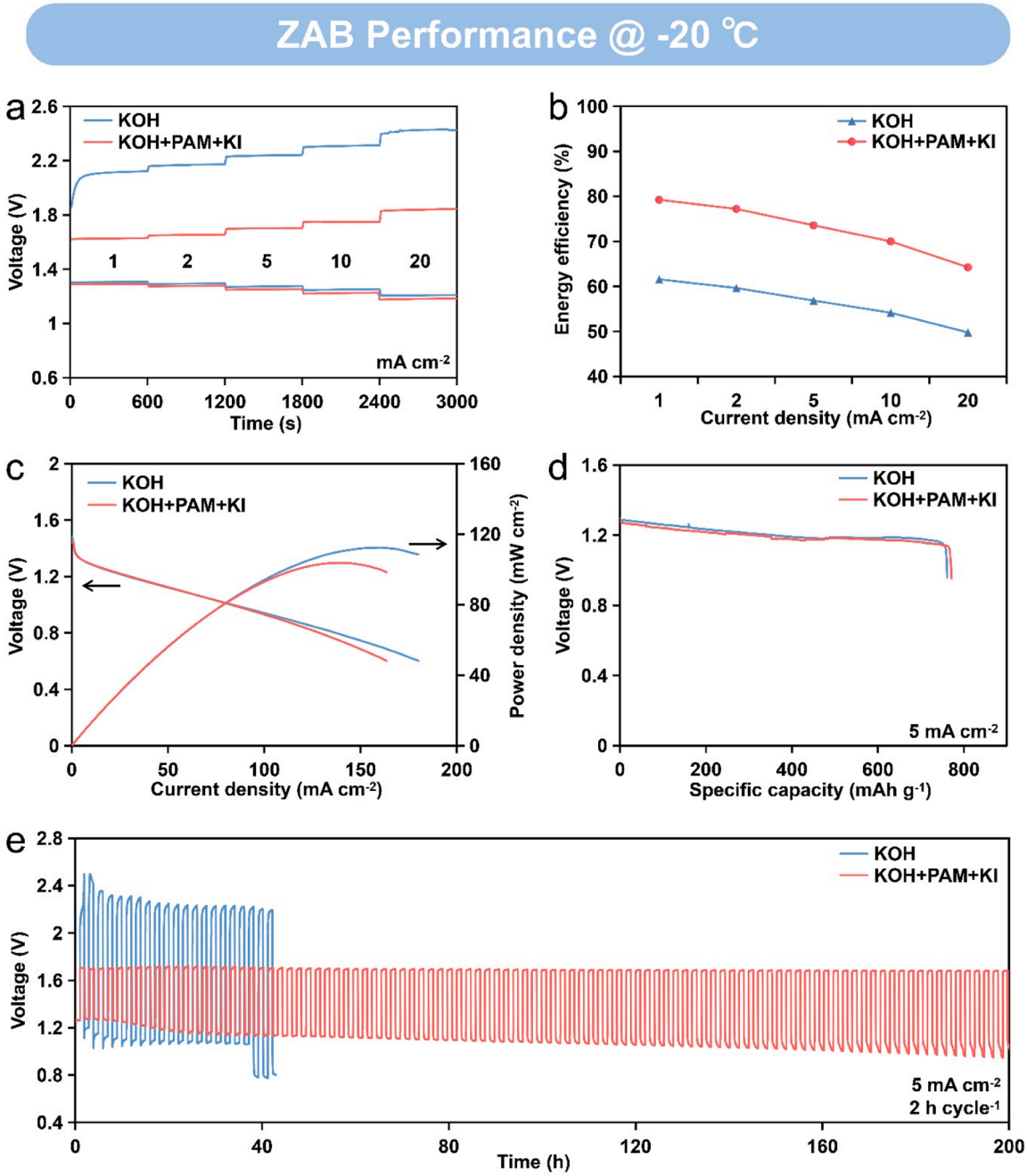

Fig. 5. Electrochemical performances of ZABs at -20 °C. (a) Charge and discharge voltages and (b) corresponding energy efficiencies at 1, 2, 5, 10, 20 mA cm^{-2}. (c) Discharge polarization profiles with corresponding power densities. (d) Discharge profiles at 5 mA cm^{-2}. (e) Galvanostatic cycling profiles at 5 mA cm^{-2} and 2 h $cycle^{-1}$. The used electrolytes are KOH and KOH + PAM + KI.

3. Conclusion

In summary, we develop a dual-additive strategy employing polymer and chaotropic anion for ZABs to realize multi-functions in suppressing parasitic HER, alleviating Zn dendrite growth, and improving battery energy efficiency. The synergistic interaction between APAM and KI proves to be more beneficial, delivering superior results compared to the use of either component independently. Consequently, the Zn-air/iodide hybrid battery exhibits an extended cycle life of 240 h with a high energy efficiency of 74.6 % and a stable Zn anode. Even in -20 °C environments, the battery maintains high performance. This strategy provides new perspectives on additive engineering and paves the way for the practical application of ZABs in energy storage.

CRediT authorship contribution statement

Siyuan Zhao: Writing – original draft, Visualization, Validation, Methodology, Investigation, Formal analysis, Data curation, Conceptualization. **Jiayu Zhao:** Writing – original draft, Validation, Investigation. **Wenlan Zhang:** Investigation. **Yaping Yan:** Investigation. **Jiachen Ma:** Writing – original draft, Investigation, Formal analysis. **Qinyang Feng:** Investigation. **Idris Temitope Bello:** Validation. **Manhui Wei:** Validation. **Tong Liu:** Writing – review & editing, Resources, Investigation. **Jinhye Bae:** Writing – review & editing, Supervision, Formal analysis. **Minshen Zhu:** Writing – review & editing, Supervision, Software, Resources, Project administration, Funding acquisition. **Meng Ni:** Writing – review & editing, Supervision, Resources, Project

administration, Investigation, Funding acquisition, Formal analysis.

Declaration of competing interest

The authors declare that they have no known competing financial interests or personal relationships that could have appeared to influence the work reported in this paper.

Data availability

Data will be made available on request.

Acknowledgement

This work is supported by the Collaborative Research Fund (CRF) (Project no. C5031-20G) of Research Grant Council, University Grants Committee, HK SAR; The European Union (ERC, SMADBINS, 101039802) and German Research Foundation DFG (ZH 989/2-1); The National Science Foundation through the University of California San Diego Materials Research Science and Engineering Center (UCSD MRSEC), Grant No. DMR-2011924; The National Nature Science Foundation of China (22209138) and Guangdong Basic and Applied Basic Research Foundation (2021A1515110464).

Supplementary materials

Supplementary material associated with this article can be found, in the online version, at doi:10.1016/j.ensm.2024.103630.

References

[1] Y. Liu, X. Lu, F. Lai, T. Liu, P.R. Shearing, I.P. Parkin, G. He, D.J. Brett, Rechargeable aqueous Zn-based energy storage devices, Joule 5 (11) (2021) 2845–2903.
[2] F. Wang, J.D. Harindintwali, Z. Yuan, M. Wang, F. Wang, S. Li, Z. Yin, L. Huang, Y. Fu, L. Li, Technologies and perspectives for achieving carbon neutrality, The Innovat. 2 (4) (2021).
[3] Y. Zhong, C. Cao, L. Zhao, M.O. Tadé, Z. Shao, Optimization of two-dimensional solid-state electrolyte–anode interface by integrating zinc into composite anode with dual-conductive phases, Green Carbon 2 (1) (2024) 94–100.
[4] L. Yang, Y.-J. Zhu, F. Zeng, H.-P. Yu, L.-Y. Dong, J. Tao, G. He, H. Li, Synchronously promoting the electron and ion transport in high-loading Mn2. 5V10O24• 5.9 H2O cathodes for practical aqueous zinc-ion batteries, Energy Storage Mater. 65 (2024) 103162.
[5] K.W. Leong, Y. Wang, M. Ni, W. Pan, S. Luo, D.Y. Leung, Rechargeable Zn-air batteries: Recent trends and future perspectives, Renew. Sustain. Energy Rev. 154 (2022) 111771.
[6] Q. Wang, S. Kaushik, X. Xiao, Q. Xu, Sustainable zinc–air battery chemistry: advances, challenges and prospects, Chem. Soc. Rev. (2023).
[7] W. Sun, F. Wang, B. Zhang, M. Zhang, V. Küpers, X. Ji, C. Theile, P. Bieker, K. Xu, C. Wang, A rechargeable zinc-air battery based on zinc peroxide chemistry, Science (1979) 371 (6524) (2021) 46–51.
[8] J.-N. Liu, C.-X. Zhao, J. Wang, D. Ren, B.-Q. Li, Q. Zhang, A brief history of zinc–air batteries: 140 years of epic adventures, Energy Environ. Sci. 15 (11) (2022) 4542–4553.
[9] Q. Liu, H. Shi, T. Han, L. Wang, H. Fu, Research progress in wide-temperature flexible zinc-air batteries, Energy Storage Mater. (2024) 103255.
[10] N. Shang, K. Wang, M. Wei, Y. Zuo, P. Zhang, H. Wang, Z. Chen, P. Pei, Challenges for large scale applications of rechargeable Zn–air batteries, J. Mater. Chem. A 10 (31) (2022) 16369–16389.
[11] J. Fu, R. Liang, G. Liu, A. Yu, Z. Bai, L. Yang, Z. Chen, Recent progress in electrically rechargeable zinc–air batteries, Adv. Mater. 31 (31) (2019) 1805230.
[12] S. Zhao, T. Liu, Y. Zuo, M. Wei, J. Wang, Z. Shao, D.Y. Leung, T. Zhao, M. Ni, High-power-density and high-energy-efficiency zinc-air flow battery system for long-duration energy storage, Chem. Eng. J. (2023) 144091.
[13] L. Yan, J. Chen, C. Yang, J. Ning, Y. Hu, Achieving high energy efficiency: recent advances in Zn-air-based hybrid battery systems, Small. Sci. (2023) 2300094.
[14] Y. Zhong, X. Xu, P. Liu, R. Ran, S.P. Jiang, H. Wu, Z. Shao, A function-separated design of electrode for realizing high-performance hybrid zinc battery, Adv. Energy Mater. 10 (47) (2020) 2002992.
[15] Q. Yang, Q. Li, Z. Liu, D. Wang, Y. Guo, X. Li, Y. Tang, H. Li, B. Dong, C. Zhi, Dendrites in Zn-based batteries, Adv. Mater. 32 (48) (2020) 2001854.
[16] D. Qiu, B. Li, C. Zhao, J. Dang, G. Chen, H. Qiu, H. Miao, A review on zinc electrodes in alkaline electrolyte: Current challenges and optimization strategies, Energy Storage Mater. (2023) 102903.
[17] Z. Xu, H. Li, Y. Liu, K. Wang, H. Wang, M. Ge, J. Xie, J. Li, Z. Wen, H. Pan, Durable modulation of Zn (002) plane deposition via reproducible zincophilic carbon quantum dots towards low N/P ratio zinc-ion batteries, Mater. Horiz. 10 (9) (2023) 3680–3693.
[18] X. Bi, Y. Jiang, R. Chen, Y. Du, Y. Zheng, R. Yang, R. Wang, J. Wang, X. Wang, Z. Chen, Rechargeable zinc–air versus lithium–air battery: from fundamental promises toward technological potentials, *Adv. Energy Mater.* 2302388.
[19] Y. Zhong, X. Xu, C. Su, M.O. Tadé, Z. Shao, Promoting bifunctional oxygen catalyst activity of double-perovskite-type cubic nanocrystallites for aqueous and quasi-solid-state rechargeable zinc-air batteries, Catalysts. 13 (10) (2023) 1332.
[20] M. Luo, W. Sun, B.B. Xu, H. Pan, Y. Jiang, Interface engineering of air electrocatalysts for rechargeable zinc–air batteries, Adv. Energy Mater. 11 (4) (2021) 2002762.
[21] L. Peng, L. Shang, T. Zhang, G.I. Waterhouse, Recent advances in the development of single-atom catalysts for oxygen electrocatalysis and zinc–air batteries, Adv. Energy Mater. 10 (48) (2020) 2003018.
[22] Z. Song, J. Ding, B. Liu, X. Liu, X. Han, Y. Deng, W. Hu, C. Zhong, A rechargeable Zn–air battery with high energy efficiency and long life enabled by a highly water-retentive gel electrolyte with reaction modifier, Adv. Mater. 32 (22) (2020) 1908127.
[23] J.-M. Assafrei, G. Yusibova, K. Ping, H.-M. Piirsoo, A. Tamm, M. Käärik, J. Leis, J. Aruväli, V. Grozovski, E. Lust, Maximizing the performance of aqueous zinc-air/iodide hybrid batteries through electrolyte composition optimization, J. Energy Storage 74 (2023) 109528.
[24] S. Zhao, T. Liu, Y. Dai, J. Wang, Y. Wang, Z. Guo, J. Yu, I.T. Bello, M. Ni, Pt/C as a bifunctional ORR/iodide oxidation reaction (IOR) catalyst for Zn-air batteries with unprecedentedly high energy efficiency of 76.5%, Appl. Catal. B: Environ. 320 (2023) 121992.
[25] H. Jiang, J. Xia, L. Jiao, X. Meng, P. Wang, C.-S. Lee, W. Zhang, Ni single atoms anchored on N-doped carbon nanosheets as bifunctional electrocatalysts for Urea-assisted rechargeable Zn-air batteries, Environmental 310 (2022) 121352.
[26] W. Xie, K. Zhu, H. Yang, W. Yang, Advancements in achieving high reversibility of zinc anode for alkaline zinc-based batteries, Adv. Mater. (2023) 2306154.
[27] Y. Zuo, K. Wang, P. Pei, M. Wei, X. Liu, Y. Xiao, P. Zhang, Zinc Dendrite Growth and Inhibition Strategies, Mater. Today Energy (2021) 100692.
[28] S. Huang, H. Li, P. Pei, K. Wang, Y. Xiao, C. Zhang, C. Chen, A dendrite-resistant zinc-air battery, iScience 23 (6) (2020).
[29] Y. Geng, L. Pan, Z. Peng, Z. Sun, H. Lin, C. Mao, L. Wang, L. Dai, H. Liu, K. Pan, Electrolyte additive engineering for aqueous Zn ion batteries, Energy Storage Mater. (2022).
[30] Q. Liu, Z. Yu, B. Zhang, Tackling the challenges of aqueous zn-ion batteries via polymer-derived strategies, Small. Methods (2023) 2300255.
[31] S. Zhao, Y. Zuo, T. Liu, S. Zhai, Y. Dai, Z. Guo, Y. Wang, Q. He, L. Xia, C. Zhi, Multi-functional hydrogels for flexible zinc-based batteries working under extreme conditions, Adv. Energy Mater. 11 (34) (2021) 2101749.
[32] X. Fan, H. Wang, X. Liu, J. Liu, N. Zhao, C. Zhong, W. Hu, J. Lu, Functionalized nanocomposite gel polymer electrolyte with strong alkaline-tolerance and high zinc anode stability for ultralong-life flexible zinc–air batteries, Adv. Mater. 35 (7) (2023) 2209290.
[33] M. Yan, N. Dong, X. Zhao, Y. Sun, H. Pan, Tailoring the stability and kinetics of Zn anodes through trace organic polymer additives in dilute aqueous electrolyte, ACS. Energy Lett. 6 (9) (2021) 3236–3243.
[34] R.S. Porter, J.F. Johnson, The entanglement concept in polymer systems, Chem. Rev. 66 (1) (1966) 1–27.
[35] M. Sun, G. Ji, J. Zheng, A hydrogel electrolyte with ultrahigh ionic conductivity and transference number benefit from Zn2+ "highways" for dendrite-free Zn-MnO2 battery, Chem. Eng. J. 463 (2023) 142535.
[36] M. Hua, S. Wu, Y. Ma, Y. Zhao, Z. Chen, I. Frenkel, J. Strzalka, H. Zhou, X. Zhu, X. He, Strong tough hydrogels via the synergy of freeze-casting and salting out, Nature 590 (7847) (2021) 594–599.
[37] K.D. Collins, M.W. Washabaugh, The Hofmeister effect and the behaviour of water at interfaces, Q. Rev. Biophys. 18 (4) (1985) 323–422.
[38] G. Cao, L. Zhao, X. Ji, Y. Peng, M. Yu, X. Wang, X. Li, F. Ran, Salting out" in hofmeister effect enhancing mechanical and electrochemical performance of amide-based hydrogel electrolytes for flexible zinc-ion battery, Small. (2023) 2207610.
[39] S. Aleid, M. Wu, R. Li, W. Wang, C. Zhang, L. Zhang, P. Wang, Salting-in effect of zwitterionic polymer hydrogel facilitates atmospheric water harvesting, ACS. Mater. Lett. 4 (3) (2022) 511–520.
[40] Y. Zhang, P.S. Cremer, Interactions between macromolecules and ions: the Hofmeister series, Curr. Opin. Chem. Biol. 10 (6) (2006) 658–663.
[41] Z. Yang, Q. Zhang, W. Li, C. Xie, T. Wu, C. Hu, Y. Tang, H. Wang, A semi-solid zinc powder-based slurry anode for advanced aqueous zinc-ion batteries, Angew. Chem. Int. Ed. 62 (3) (2023) e202215306.
[42] Y. Wang, Q. Li, H. Hong, S. Yang, R. Zhang, X. Wang, X. Jin, B. Xiong, S. Bai, C. Zhi, Lean-water hydrogel electrolyte for zinc ion batteries, Nat. Commun. 14 (1) (2023) 3890.
[43] Y. Pei, L. Zhao, G. Du, N. Li, K. Xu, H. Yang, Investigation of the degradation and stability of acrylamide-based polymers in acid solution: Functional monomer modified polyacrylamide, Petroleum 2 (4) (2016) 399–407.
[44] Q. Zhang, J. Luan, L. Fu, S. Wu, Y. Tang, X. Ji, H. Wang, The three-dimensional dendrite-free zinc anode on a copper mesh with a zinc-oriented polyacrylamide electrolyte additive, Angewandte Chemie Internat. Edit. 58 (44) (2019) 15841–15847.
[45] S. Zhao, K. Wang, S. Tang, X. Liu, K. Peng, Y. Xiao, Y. Chen, A new solid-state zinc–air battery for fast charge, Energy Techn. 8 (5) (2020) 1901229.

[46] M.J. Tan, B. Li, P. Chee, X. Ge, Z. Liu, Y. Zong, X.J. Loh, Acrylamide-derived freestanding polymer gel electrolyte for flexible metal-air batteries, J. Power Sour. 400 (2018) 566–571.
[47] S. Wu, M. Hua, Y. Alsaid, Y. Du, Y. Ma, Y. Zhao, C.Y. Lo, C. Wang, D. Wu, B. Yao, Poly (vinyl alcohol) hydrogels with broad-range tunable mechanical properties via the Hofmeister effect, Adv. Mater. 33 (11) (2021) 2007829.
[48] B. Luo, C. Cai, T. Liu, X. Meng, X. Zhuang, Y. Liu, C. Gao, M. Chi, S. Zhang, J. Wang, Multiscale structural nanocellulosic triboelectric aerogels induced by hofmeister effect, Adv. Funct. Mater. 33 (42) (2023) 2306810.
[49] S. Zhao, T. Liu, Y. Dai, Y. Wang, Z. Guo, S. Zhai, J. Yu, C. Zhi, M. Ni, All-in-one and bipolar-membrane-free acid-alkaline hydrogel electrolytes for flexible high-voltage Zn-air batteries, Chem. Eng. J. 430 (2022) 132718.
[50] Q. Zhang, K. Xia, Y. Ma, Y. Lu, L. Li, J. Liang, S. Chou, J. Chen, Chaotropic anion and fast-kinetics cathode enabling low-temperature aqueous Zn batteries, ACS. Energy Lett. 6 (8) (2021) 2704–2712.
[51] Q. Jian, T. Wang, J. Sun, B. Liu, T. Zhao, Hydrated solvation suppression of zinc ions for highly reversible zinc anodes, Chem. Eng. J. 466 (2023) 143189.
[52] S. Huang, L. Hou, T. Li, Y. Jiao, P. Wu, Antifreezing hydrogel electrolyte with ternary hydrogen bonding for high-performance zinc-ion batteries, Adv. Mater. 34 (14) (2022) 2110140.
[53] B. Youbi, Y. Lghazi, M.A. Himi, A. Aynaou, J. Bahar, C. El Haimer, A. Ouedrhiri, A. Sahlaoui, I. Bimaghra, Electrochemical and structural investigation of BixTey thin films electrodeposited on ITO substrate, Appl. Surface Sci. Adv. 16 (2023) 100419.
[54] L. Cao, D. Li, E. Hu, J. Xu, T. Deng, L. Ma, Y. Wang, X.-Q. Yang, C. Wang, Solvation structure design for aqueous Zn metal batteries, J. Am. Chem. Soc. (2020).
[55] J.E. Baur, Diffusion coefficients, Handbook of electrochemistry, Elsevier, 2007, pp. 829–848.
[56] S. Zhao, T. Liu, Y. Wang, Z. Guo, I.T. Bello, Q. He, Y. Zuo, M. Wei, M. Ni, Innovating rechargeable Zn-Air batteries for low charging voltage and high energy efficiency, Energy Fuels (2022).
[57] H.S. Fan, X. Liang, F.X. Ma, G. Zhang, Z.Q. Liu, L. Zhen, X.C. Zeng, C.Y. Xu, Low-potential iodide oxidation enables dual-atom CoFe- N- C catalysts for ultra-stable and high-energy-efficiency Zn-Air batteries, Small. (2023) 2307863.
[58] Z. Pei, Z. Yuan, C. Wang, S. Zhao, J. Fei, L. Wei, J. Chen, C. Wang, R. Qi, Z. Liu, A flexible rechargeable zinc–air battery with excellent low-temperature adaptability, Angewandte Chemie. Internat.l Edit. 59 (12) (2020) 4793–4799.
[59] C.X. Zhao, J.N. Liu, N. Yao, J. Wang, D. Ren, X. Chen, B.Q. Li, Q. Zhang, Can aqueous zinc–air batteries work at sub-zero temperatures? Angew. Chem. 133 (28) (2021) 15409–15413.